MATERIALS PHYSICS AND MECHANICS RESEARCH ARTICLE

Submitted: September 11, 2025 **Revised: October 29, 2025** **Accepted: December 4, 2025**

Dynamic effects of a hollow cylinder quasi-force-free magnet

M.I. Lobachev ✉

Peter the Great Saint-Petersburg Polytechnic University, St. Petersburg, Russia

✉ lobachev_mi@spbstu.ru

ABSTRACT

This study investigates mechanical stresses induced by a unipolar sinusoidal pulse in a hollow cylindrical conductor, which serves as a key element of the base part of a quasi-force-free configuration pulsed magnet. The aim of the work is to assess transient mechanical effects not accounted for by static models. The applied method determines the system's natural frequencies and solves the dynamic axisymmetric problem of elasticity theory using Laplace transforms. The results include the calculated spectrum of natural frequencies; it is shown that the stress response exhibits quasistatic behavior for millisecond-duration pulses, whereas dangerous stress magnification requires microsecond pulses which are consistent with the single-degree-of-freedom model predictions. In conclusion, the adequacy of static models for designing magnets with millisecond-range pulses is confirmed, and the development of a methodology for analyzing complex multilayer magnets is proposed.

KEYWORDS

quasi-force-free magnet • hollow cylinder • dynamic response • Lorentz force • von Mises stress • natural frequencies pulsed magnetic field

Citation: Lobachev MI. Dynamic effects of a hollow cylinder quasi-force-free magnet. *Materials Physics and Mechanics*. 2026;54(2): 57–69.
http://dx.doi.org/10.18149/MPM.5422026_5

Introduction

Strong and ultra-strong magnetic fields are vital research tools with applications spanning from the study of fundamental material properties [1–3] to magnetic resonance imaging (MRI) [4,5], magnetic pulse forming [6], plasma confinement in fusion energy research [7–10]. The generation of such fields presents significant engineering challenges, primarily related to material strength and thermal management. Consequently, for sustained laboratory research, non-destructive methods are paramount. Through a variety of non-destructive methods presented in [11] (Fig. 1) we are interested in the highest magnetic fields – short-pulsed facilities. While state-of-the-art pulsed magnets, often based on the force-balanced coil principle, have achieved fields in the 80–100 T range, the quest for higher fields faces significant technological barriers. The primary limitations are Joule heating and mechanical stresses induced by the Lorentz force.

The force-balanced coil technique, employed in leading laboratories (Germany [12], China [13], France [14]), is designed to manage mechanical stress by distributing Lorentz forces evenly across a complex, multi-layer winding structure. A landmark achievement of this approach was the generation of a 100.75 T field [15] in Los Alamos, USA. However, this methodology carries a critical and inherent limitation: the exponential scaling of the magnet's size and mass with the target field strength. This relationship is described by the ratio of the external radius to the inner radius $\frac{R_e}{R_i} \sim exp(1 / \eta_{max})$, where η_{max} is

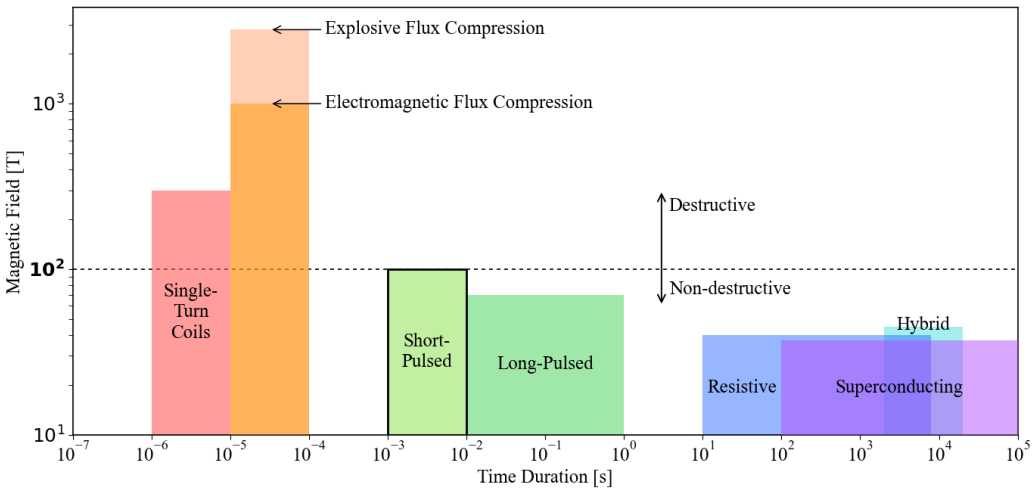

Fig. 1. Overview of strong-magnetic fields generation methods. Based on data from [11]

a dimensionless stress parameter (von Mises stress divided by magnetic pressure $B_0^2/2\mu_0$), implies that advancing beyond current records would require magnets of prohibitively large dimensions and immense stored energy, rendering this path economically and practically unviable for many applications.

This impasse has spurred the investigation of alternative paradigms, among which the "quasi-force-free" magnet concept ([16–21]) presents a promising solution. Its principle is to engineer the current density vector $\underline{J}$ to be nearly parallel to the internal magnetic field $\underline{B}$ within the conductor, thereby minimizing the Lorentz force density ($\underline{J} \times \underline{B}$). This is achieved through a specific configuration of toroidal and poloidal current components that promote force self-compensation.

As a basic element of a quasi-force-free magnet, a solenoid with a specific winding angle can be considered (Fig. 2(a)). Such a structure may be approximated as an infinitely long hollow cylinder with inner radius R_1 and outer radius R_2 in an axisymmetric representation (Fig. 2(b)). The winding angle is directly related to the azimuthal magnetic

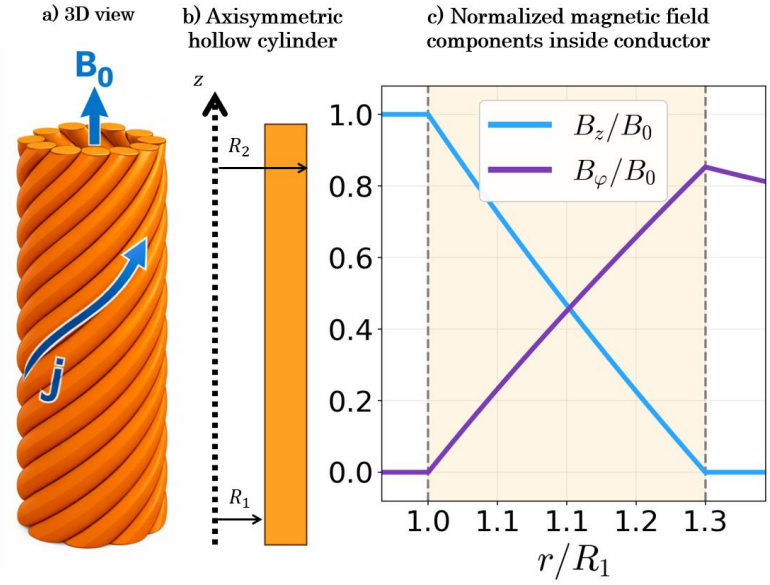

Fig. 2. Basic element of a quasi-force-free magnet

field B_φ. A typical spatial distribution of the magnetic field components $\underline{B}$ is shown in Fig. 2(c) and calculated, for example, in [22].

Existing theoretical analyses of the central base region usually use simplified static models to estimate the stress at the peak of the current pulse. While this approach provides a useful reference point, it does not account for the transient dynamics that occur during real pulsed operation. In practice, the pulse duration and the electromagnetic skin effect characterized by the ratio of the conductor thickness to the skin depth play a key role. They determine how the current, and therefore the volumetric Lorentz force, is distributed inside the conductor. This time-varying force distribution ultimately governs the conductor's dynamic mechanical response.

The present work addresses this gap by investigating non-stationary processes in a fundamental single-layer cylindrical model of a quasi-force-free magnet. The analysis follows a sequential methodology. First, the natural vibration frequencies of a hollow cylinder are determined. Subsequently, the dynamic problem of linear elasticity theory is solved under the action of a previously calculated balancing volumetric radial force. This force results from a unipolar current pulse in the form of a half-wave sine. Due to the linearity of the problem, the effects of electromagnetic diffusion (which determines the force profile) can be considered separately from the dynamic mechanical effects. This article is specifically devoted to the latter, as indicated by its title.

Methods

The research methodology for analyzing the dynamic mechanical response of a quasi-force-free magnet conductor is based on a sequential solution of two coupled physical problems: determining the natural vibrational spectrum of the system and calculating its forced oscillations under a given electromagnetic load. The method is described in such detail that it can be reproduced to obtain similar results.

Analytical model and governing equations

The object of study is an infinitely long, hollow, isotropic cylindrical conductor with inner radius R_1 and outer radius R_2. The analysis is conducted within the framework of linear elasticity theory under axisymmetric plane strain conditions. The radial displacement $u(r,t)$ is the primary variable. The starting point is the equation of motion for radial vibrations, derived from the balance of linear momentum:

$$\rho\frac{\partial^2 u}{\partial t^2} = c_{11}\frac{\partial}{\partial r}\left(\frac{\partial u}{\partial r}+\frac{u}{r}\right), \quad (1)$$

where ρ is the material density, and $c_{11} = \lambda + 2\mu$ is an elastic modulus (λ and μ are Lamé constants). Introducing the speed of the dilatational wave $c = \sqrt{\frac{c_{11}}{\rho}}$ simplifies the equation to:

$$\frac{\partial^2 u}{\partial t^2} = c^2\frac{\partial}{\partial r}\left(\frac{\partial u}{\partial r}+\frac{u}{r}\right). \quad (2)$$

To find the natural frequencies, a free vibration problem is considered. A solution to Eq. (2) is sought in the form:

$$u(r,t) = U(r)exp(j\omega_n t), \quad (3)$$

were $\omega_n$is the angular natural frequency and $U(r)$ describes the radial mode shape. Substituting this form into the governing equation leads to an ordinary differential equation for the spatial amplitude:

$$\frac{d^2U}{dr^2} + \frac{1}{r}\frac{dU}{dr} + \left(\frac{\omega_n^2}{c^2} - \frac{1}{r^2}\right)U = 0. \tag{4}$$

Equation (4) is a canonical form of Bessel's differential equation. Its general solution is a linear combination of first-order Bessel functions of the first and second kind:

$$U(r) = C_1 J_1\left(\frac{\omega_n r}{c}\right) + C_2 Y_1\left(\frac{\omega_n r}{c}\right), \tag{5}$$

where C_1 and C_2 are constants determined by the boundary conditions.

Determination of natural frequencies and modes

For a free-standing cylinder with no external traction on its inner R_1 and outer R_2 surfaces, the radial stress σ_r must vanish at both boundaries. The radial stress for a plane strain case is given by:

$$\sigma_r = c_{11}\frac{\partial u}{\partial r} + \lambda\frac{u}{r}. \tag{6}$$

Introducing a parameter $m = \lambda/c_{11}$, the boundary conditions can be expressed as:

$$\begin{aligned}\left(\frac{dU}{dr} + m\frac{U}{r}\right)\Big|_{r=R_1} &= 0,\\ \left(\frac{dU}{dr} + m\frac{U}{r}\right)\Big|_{r=R_2} &= 0.\end{aligned} \tag{7}$$

Substituting the general solution from Eq. (5) into these boundary conditions yields a system of two homogeneous linear equations for C_1 and C_2. For a non-trivial solution to exist, the determinant of the coefficient matrix must be zero. This requirement leads to the following characteristic equation, the solutions of which define the discrete set of natural frequencies ω_n of the system:

$$\begin{aligned}&\left[\frac{\omega_n R_1}{c}J_0\left(\frac{\omega_n R_1}{c}\right) + (m-1)J_1\left(\frac{\omega_n R_1}{c}\right)\right]\left[\frac{\omega_n R_2}{c}Y_0\left(\frac{\omega_n R_2}{c}\right) + (m-1)Y_1\left(\frac{\omega_n R_2}{c}\right)\right] -\\ &\left[\frac{\omega_n R_2}{c}J_0\left(\frac{\omega_n R_2}{c}\right) + (m-1)J_1\left(\frac{\omega_n R_2}{c}\right)\right]\left[\frac{\omega_n R_1}{c}Y_0\left(\frac{\omega_n R_1}{c}\right) + (m-1)Y_1\left(\frac{\omega_n R_1}{c}\right)\right] = 0.\end{aligned} \tag{8}$$

To simplify the numerical solution of Eq. (8), it is convenient to introduce the dimensionless frequency $\hat{\omega}_n = \omega_n R_1/c$ and the geometry ratio $g = R_2/R_1$. The boundary condition terms can be compactly defined as:

$$\begin{aligned}\mathcal{A}_{11}(\hat{\omega}) &= (m-1)J_1(\hat{\omega}) + \hat{\omega}J_0(\hat{\omega}),\\ \mathcal{A}_{12}(\hat{\omega}) &= (m-1)Y_1(\hat{\omega}) + \hat{\omega}Y_0(\hat{\omega}),\\ \mathcal{A}_{21}(\hat{\omega}, g) &= (m-1)J_1(g\hat{\omega}) + g\hat{\omega}J_0(g\hat{\omega}),\\ \mathcal{A}_{22}(\hat{\omega}, g) &= (m-1)Y_1(g\hat{\omega}) + g\hat{\omega}Y_0(g\hat{\omega}).\end{aligned} \tag{9}$$

The characteristic equation then reduces to the vanishing of a $2x2$ determinant:

$$\mathcal{A}_{11}(\hat{\omega})\cdot\mathcal{A}_{22}(\hat{\omega}, g) - \mathcal{A}_{12}(\hat{\omega})\cdot\mathcal{A}_{21}(\hat{\omega}, g) = 0. \tag{10}$$

The roots $\hat{\omega}_n$ of Eq. (10) correspond to the dimensionless eigenfrequencies of the hollow cylinder. The results match with works in [23], in [24] for isotropic case and with the case of axially symmetric vibrations in [25].

Dynamic response to electromagnetic loads

Having established the natural frequencies of the force-free cylinder, we now proceed to model its dynamic response when subjected to the transient volumetric Lorentz forces generated during a current pulse. The governing equation now:

$$\rho \frac{\partial^2 u}{\partial t^2} = c_{11}\left(\frac{\partial^2 u}{\partial r^2} + \frac{1}{r}\frac{\partial u}{\partial r} - \frac{u}{r^2}\right) + f(r,t), \tag{11}$$

where $f(r,t) = X(r)\sin(\omega_d t)$ in particular case modeled as a half-wave sine pulse with driven frequency ω_d and active time $t\ \epsilon\ [0, \frac{T}{2}]$.

To solve this non-homogeneous partial differential equation, we employ the Laplace transform with respect to time. The transform of the displacement is defined as $U_L(r,s) = \mathcal{L}\{u(r,t)\}$. Applying the transform to Eq. (11), and assuming zero initial displacement and velocity, yields:

$$\left(\frac{d^2 U_L}{dr^2} + \frac{1}{r}\frac{dU_L}{dr} - \frac{U_L}{r^2}\right) - \frac{s^2}{c^2}U_L = F_L, \tag{12}$$

where the transformed forcing function is:

$$F_L = -\frac{\mathcal{L}\{f(r,t)\}}{c_{11}} = -\frac{X(r)}{c_{11}} \cdot \frac{\omega_d}{s^2+\omega_d^2}. \tag{13}$$

The general solution in the Laplace domain is the sum of homogeneous and particular solutions:

$$U_L(r,s) = U_L^{(h)}(r,s) + U_L^{(p)}(r,s). \tag{14}$$

The homogeneous solution is expressed in terms of modified Bessel functions:

$$U_L^{(h)}(r,s) = C_1(s)I_1\left(\frac{s}{c}r\right) + C_2(s)K_1\left(\frac{s}{c}r\right). \tag{15}$$

A particular solution is found using the method of variation of parameters, involving integrals of the form:

$$\begin{aligned} \widehat{C_1}(r,s) &= \int_{R_1}^{r} \xi F_L(\xi,s)K_1\left(\frac{s}{c}\xi\right)d\xi, \\ \widehat{C_2}(r,s) &= -\int_{R_1}^{r} \xi F_L(\xi,s)I_1\left(\frac{s}{c}\xi\right)d\xi. \end{aligned} \tag{16}$$

So, it can be constructed by:

$$U_L^{(p)}(r,s) = \widehat{C_1}(r,s)I_1\left(\frac{s}{c}r\right) + \widehat{C_2}(r,s)K_1\left(\frac{s}{c}r\right). \tag{17}$$

Constants $C_1(s)$, $C_2(s)$ are determined by applying the traction-free boundary conditions similarly to Eq. (10) to the full solution $U_L(r,s)$, which leads to a linear algebraic system solved for each complex s:

$$\mathcal{M} \cdot \begin{bmatrix} C_1(s) \\ C_2(s) \end{bmatrix} = b. \tag{18}$$

where matrix $\mathcal{M}$ and vector b coefficients are:

$$\begin{aligned} \mathcal{M}_{11} &= \frac{(m-1)}{R_1}I_1\left(\frac{s}{c}R_1\right) + \frac{s}{c}I_0\left(\frac{s}{c}R_1\right), \\ \mathcal{M}_{12} &= \frac{(m-1)}{R_1}K_1\left(\frac{s}{c}R_1\right) + \frac{s}{c}K_0\left(\frac{s}{c}R_1\right), \\ \mathcal{M}_{21} &= \frac{(m-1)}{R_2}I_1\left(\frac{s}{c}R_2\right) + \frac{s}{c}I_0\left(\frac{s}{c}R_2\right), \\ \mathcal{M}_{22} &= \frac{(m-1)}{R_2}K_1\left(\frac{s}{c}R_2\right) + \frac{s}{c}K_0\left(\frac{s}{c}R_2\right), \\ b_1 &= 0, \\ b_2 &= -\left[\widehat{C_1}(R_2,s)\mathcal{M}_{21} + \widehat{C_2}(R_2,s)\mathcal{M}_{22}\right]. \end{aligned} \tag{19}$$

The final time-domain solution $u(r,t)$ is obtained by numerical inversion of the Laplace transform (e.g., using the Gaver-Stehfest algorithm [26]).

Quasi-force-free magnet implementation

The methodology described in the previous sections is applied to a specific quasi-force-free magnet configuration (Fig. 2). The volumetric force distribution $X(r)$ is selected to

satisfy the self-equilibration condition, ensuring zero net radial force through the conductor wall [22]:

$$\int_{R_1}^{R_2} X(r)dr = 0. \quad (20)$$

Thus, the expression is:

$$X(r) = \mu_0 \left(\frac{A_1^2}{r}\ln\left(\frac{R_2}{r}\right) + \frac{Z_1^2}{2}\cdot\frac{R_1^2 - r^2}{r}\right), \quad (21)$$

where μ_0 is the magnetic constant. Constants A_1, Z_1 are defined by the target central magnetic field B_0 and geometry:

$$A_1 = \frac{B_0}{\mu_0 \ln(g)}, Z_1 = \frac{2B_0\theta R_2}{\mu_0(R_2^2 - R_1^2)}. \quad (22)$$

The parameter $\theta = B_p/B_0$ (ratio of poloidal to axial field) is calculated as:

$$\theta = \frac{g^2-1}{2g\sqrt{\frac{g^2-1}{2} - \ln(g)}}. \quad (23)$$

It is important to emphasize that in the present formulation the radial force distribution $X(r)$ is prescribed. Electromagnetic diffusion and possible redistribution of current density are intentionally excluded from the model. The spatial profile given by Eq. (21) is treated as a fixed load satisfying the self-equilibration condition, while the temporal dependence is introduced solely through the harmonic factor $\sin(\omega_d t)$.

The analytical solution obtained in the previous sections is formulated for an arbitrary self-equilibrated function $X(r)$. Therefore, it is not restricted to the idealized hollow cylindrical geometry assumed here. In practical conductors, the actual cross-section (e.g., a round wire in a tightly wound helix) does not form a perfectly rectangular r-z domain. This geometric difference may modify the detailed spatial distribution of the Lorentz force; however, it does not alter the structure of the dynamic problem itself. The mechanical response is governed primarily by the excitation frequency relative to the eigenfrequencies of the system, whereas moderate variations of the radial load shape affect only quantitative details of the response amplitude.

Results and Discussion

The developed analytical and numerical model was applied to analyze the dynamic mechanical response of a quasi-force-free magnet conductor with specific geometric and material parameters. The aim was to assess the stress levels under a high magnetic field pulse and identify potential risks of stress amplification. The geometric ratio was set at $g = R_2/R_1 = 1.3$, and the conductor material was modeled with properties typical of beryllium bronze: Young's modulus $E = 131$ GPa, Poisson's ratio $\nu = 0.3$, and density $\rho = 8900\ \mathrm{kg/m^3}$. The target central magnetic field was $B_0 = 100$ T.

In the dynamic analysis, the excitation frequency of the current pulse becomes a critical parameter. The electromagnetic skin effect is characterized by the dimensionless parameter $k = \Delta/\Delta_0$ defined [27] as the ratio of the conductor thickness $\Delta = R_2 - R_1$ and the skin depth:

$$\Delta_0 = \sqrt{\frac{2}{\sigma\mu_0\omega_d}}. \quad (24)$$

Here, σ is the electrical conductivity and ω_d is associated with the current pulse duration. It should be noted that Eq. (19) is only applicable for weak skin-effect regime ($k \leq 1$). In this case, the electromagnetic diffusion time is sufficiently long to ensure

nearly uniform current distribution across the conductor wall, thereby validating the assumption of a spatially constant force profile during the dynamic excitation.

Natural vibration spectrum

The solution of the characteristic equation (10) yielded the dimensionless eigenfrequencies of the hollow cylindrical conductor. Graphic representation of the numerical solution in Matlab for Eq. (10) is presented in Fig. 3.

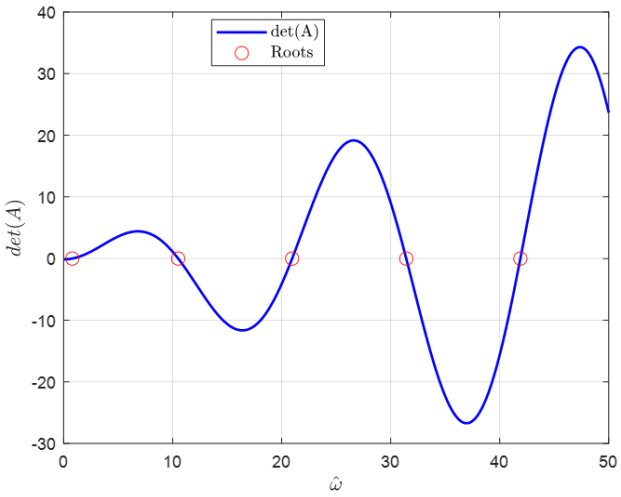

Fig. 3. Roots of Eq. (10) for determination of natural frequencies

The first fundamental dimensionless frequency was found to be $\widehat{\omega_1} \approx 0.797$. In the present formulation, the excitation is introduced as a $f(r,t) = X(r)\sin(\omega_d t)$, and the frequency parameter is conveniently expressed through the dimensionless quantity k via:

$$\omega_d = \frac{2k^2}{\sigma\mu_0\Delta^2}. \tag{25}$$

Using this relation purely as a parametrization of the excitation frequency, we determine the value of k for which the driving frequency coincides with the first eigenfrequency. For beryllium bronze ($\sigma = 60$ MS/m) yields $k \approx 10.971$. This value lies well above the operational regime considered here and corresponds to pulse durations in the microsecond range ($\tau = \pi/\omega_d$).

Dynamic stress response

For the stress response analysis, stress tensor components are calculated using constitutive relations for isotropic linear elasticity under plane strain:

$$\begin{aligned}\sigma_r(r,t) &= c_{11}\frac{\partial u}{\partial r} + \lambda\frac{u}{r},\\ \sigma_\varphi(r,t) &= \lambda\frac{\partial u}{\partial r} + c_{11}\frac{u}{r},\\ \sigma_z(r,t) &= \lambda\left(\frac{\partial u}{\partial r} + \frac{u}{r}\right).\end{aligned} \tag{26}$$

The von Mises equivalent stress is:

$$\sigma_{Mis}(r,t) = \sqrt{\frac{1}{2}\left[\left(\sigma_r - \sigma_\varphi\right)^2 + \left(\sigma_\varphi - \sigma_z\right)^2 + \left(\sigma_z - \sigma_r\right)^2\right]}. \tag{27}$$

The dynamic response to a half-sine current pulse was calculated for various skin-effect regimes (*k* values). Figure 4 illustrates the spatial-temporal evolution of the

normalized radial displacements $u(r,t)/R_1$ and von Mises stress $\eta(r,t) = 2\mu_0\sigma_{Mis}(r,t)/B_0^2$ for a representative case with $k = 0.5$. The stress rises smoothly following the temporal profile of the driving pulse, consistent with a linear system in a regime far from first natural frequency. The peak stress values align well with those predicted by static analyses for comparable geometries [22], confirming the model's validity in the quasi-stationary limit ($k \leq 1$) at the peak of the pulse ($t = T/4$).

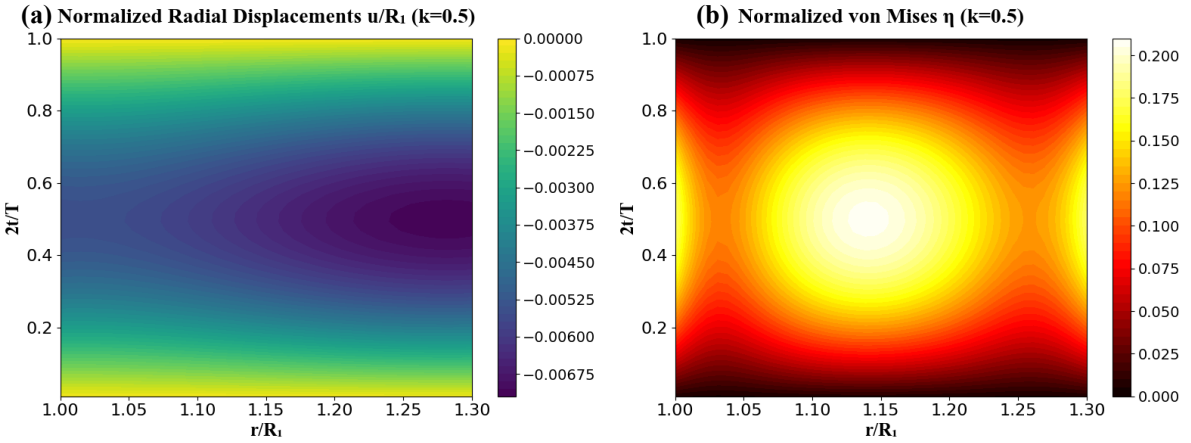

Fig. 4. Normalized contour plots of radial displacements (a) and von Mises (b) stresses for *k* = 0.5

A critical aspect of pulsed magnet operation is the dynamic mechanical response, which becomes significant when the characteristic timescale of the electromagnetic excitation is comparable to the natural mechanical periods of the conductor. In this analysis, this regime is explored by varying the normalized parameter k, which here scales the angular frequency ω_d of the applied half-sine force pulse. The prescribed spatial force distribution $X(r)$, corresponding to the quasi-force-free equilibrium, remains unchanged; the parameter k thus serves as a normalized driving frequency, $k \propto \sqrt{\omega_d}$, controlling the rate of load application.

The system's dynamic response is highly sensitive to the relationship between this driving frequency and the conductor's natural eigenfrequencies. For low k, the stress develops quasi-statically, and the peak von Mises stress η corresponds to the static solution.

With increasing values of the dimensionless parameter k, the inertial forces within the conductor become significant, causing the system's response to transition from a quasi-static to a genuinely dynamic regime. This transition is characterized by a pronounced frequency-dependent amplification of the mechanical fields, as detailed in Fig. 5.

Figure 5 presents the normalized dynamic response of the hollow cylinder to impulsive loading across a range of k values. Subfigure 5(a) shows the dynamic amplification factor for radial displacement, defined as $\frac{max|u_r(r,t)|}{\max|u_{st}|}$ through the whole impulse time, where $\max|u_{st}|$ is the maximum amplitude of radial displacements for quasi-static solution or $max\left|u_r\left(r,\frac{T}{4}\right)\right|$ for lower k. Subfigures 5(b) and 5(c) depict the normalized time and radial coordinate for $max|u_r(r,t)|$ during impulse time. Finally, subfigure 5(d) illustrates the corresponding dynamic amplification factor for the stress measure given by $\frac{\max\eta(r,t)}{\max\eta_{static}}$.

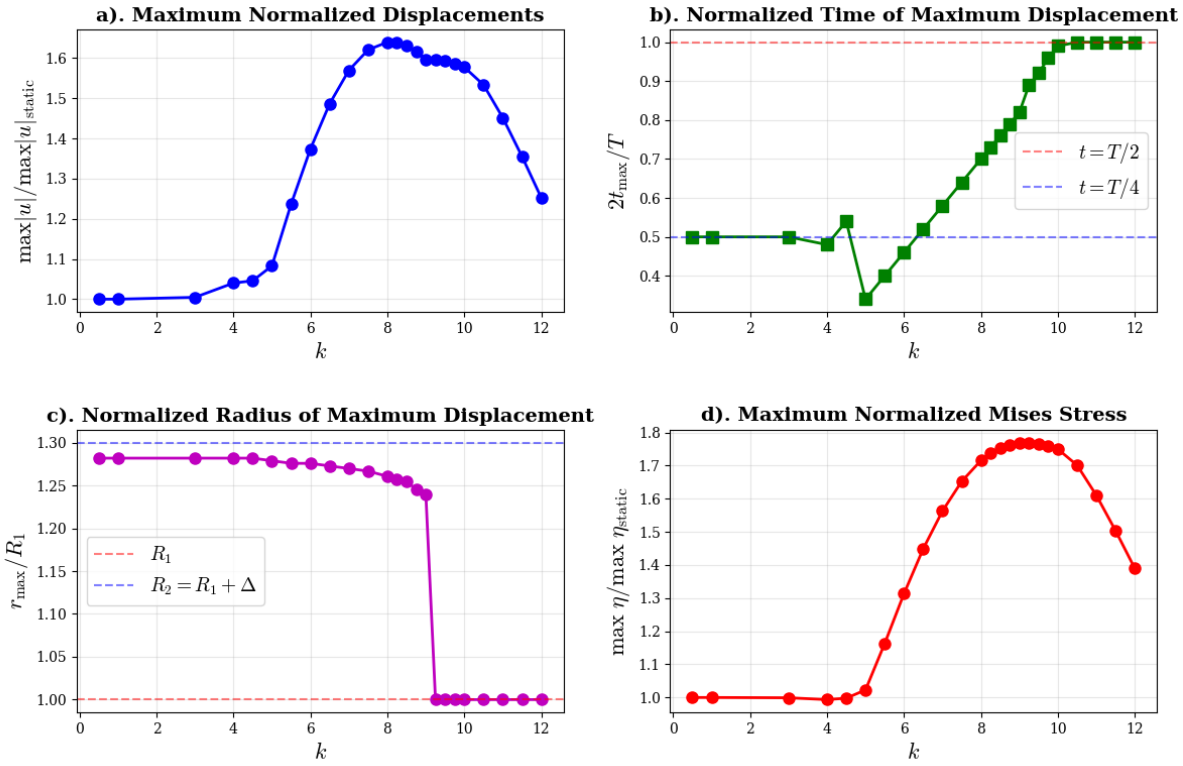

Fig. 5. Normalized mechanical values dependences from k: (a) $\frac{max|u_r(r,t)|}{\max|u_{static}|}$, (b) time corresponds to $max|u_r(r,t)|$ normalized to pulse time, (c) radial coordinate corresponds to $max|u_r(r,t)|$ normalized to inner radius, (d) $\frac{\max\eta(r,t)}{\max\eta_{static}}$

To elucidate the observed dynamic behavior, it is instructive to draw an analogy with the classical single-degree-of-freedom (SDOF) system. The response-ration time history is $R(t) = u_{SDOF}(t)/(\frac{p_0}{k_{SDOF}})$ of an undamped SDOF system subjected to a harmonic load $p_0 \sin\bar{\omega}t$, starting from the rest, is governed by:

$$m_{SDOF}\ddot{u}_{SDOF}(t) + k_{SDOF}u_{SDOF}(t) = p_0 \sin\bar{\omega}t. \quad (28)$$

Introducing the frequency ratio $\beta = \frac{\bar{\omega}}{\omega_{SDOF}} = \bar{\omega}\sqrt{\frac{m_{SDOF}}{k_{SDOF}}}$, the solution can be expressed as:

$$R(t) = \frac{1}{1-\beta^2}(\sin\bar{\omega}t - \beta\sin\omega_{SDOF}t). \quad (29)$$

For case of single half-sine impulse loading it is convenient to introduce $\alpha = t/\tau$, where $\tau = T/2$ is the end time point. Then, Eq. (26) will be:

$$R(\alpha) = \frac{1}{1-\beta^2}(\sin\pi\alpha - \beta\sin\frac{\pi\alpha}{\beta}),\ 0 \le \alpha \le 1. \quad (30)$$

Here introduced β can be rewritten in terms of ω_d (or k) as $\bar{\omega}$ and our found first natural frequency as ω_{SDOF}. In Fig. 6, the time-dependent response-ration for different values of k and corresponding β can be seen.

It can be seen that for k in operational regime ($\beta \le 0.008$) response-ratio curve will approach the quasi-static response curve. Starting from $k \approx 5$ the second term of Eq. (30) becomes significant, and the first peak corresponds to maximum response-ratio. The time

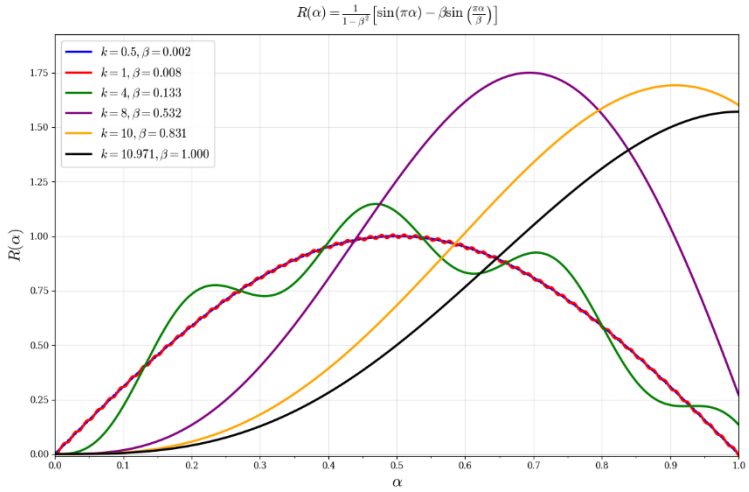

Fig. 6. Single degree-of-freedom response-ration time history representation for different k

α_{max} of this first maximum, found by taking the derivative and solving $dR(\alpha)/d\alpha = 0$, is given by:

$$\alpha_{max} = \frac{2\beta}{\beta+1}, \ 0 \le \alpha \le 1. \tag{31}$$

The dependence of α_{max} on k, plotted in Fig. 7, explains the trend observed in Fig. 5(b): the instant of maximum displacement shifts with increasing k. It reaches $\alpha_{max} = 1$ at $\beta = 1$ ($k \approx 10.971$), that means that driven frequency of impulse becomes equal to the first natural frequency of the system.

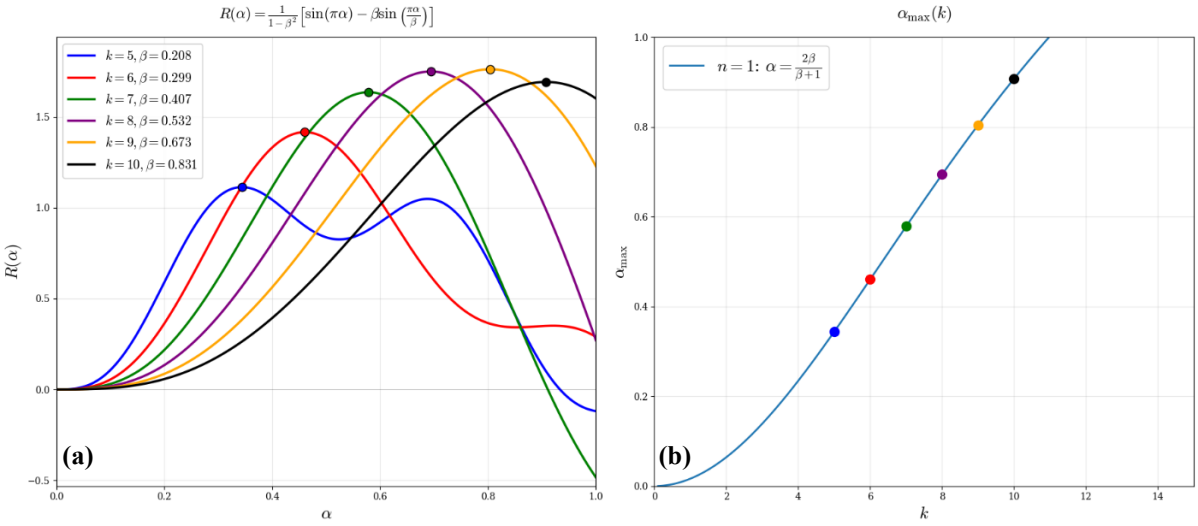

Fig. 7. Maximum single degree-of-freedom response-ration time history representation for different k (a) and corresponding normalized times of maximum (b)

The analytical model of the hollow cylinder (Fig. 5) reveals a decrease in the maximum recorded displacement and stress for k values beyond the resonant point ($\beta > 1$). This occurs because the simulation time is limited to the impulse duration τ. At higher k, the maximum system response may occur during the subsequent free-vibration phase, governed by the displacement $u(r,\tau)$ and the velocity $\dot{u}(r,\tau)$ conditions at time τ. Although the absolute maximum *during the impulse* does not peak precisely at $\beta = 1$

in either the SDOF or the cylinder model, the resonant condition $\beta = 1$ yields the largest amplitude of *free vibrations* after the load is removed. This post-impulse response is critical for assessing potential fatigue damage and the structural integrity of the conductor under repeated loading.

Conclusions

The dynamic analysis of a hollow cylindrical quasi-force-free magnet conductor subjected to a transient electromagnetic pulse yields the following principal conclusions:

1. The natural vibrational spectrum of a free, hollow cylindrical conductor has been determined analytically. For a typical geometry ratio ($g = 1.3$), the fundamental dimensionless eigenfrequency is $\widehat{\omega_1} \approx 0.797$.

2. A dynamic model has been developed, solving the forced mechanical response to a prescribed volumetrically distributed Lorentz force via Laplace transforms techniques. It is critical to note that this analysis decouples the mechanical dynamics from the electromagnetic diffusion process; the spatial force profile $X(r)$ is assumed from a static quasi-force-free equilibrium and is not recalculated during the pulse. This model provides complete time-dependent displacement and stress fields for an arbitrary pulse shape.

3. The system's response is governed by the ratio of the pulse driving frequency to the fundamental natural frequency, analogous to the frequency ratio β in a single-degree-of-freedom (SDOF) system. For the operational regime with millisecond pulses ($k \leq 1$, $\beta \ll 1$), the response is quasi-static, and peak stresses align with static model predictions.

4. A transition to a genuinely dynamic regime occurs for microsecond ([28–31]) pulses ($k > 1$, $\beta \to 1$), characterized by frequency-dependent amplification and a shift in the time of peak response within the pulse duration, as accurately predicted by the SDOF analogy. The most severe dynamic amplification of stresses (exceeding static levels by a factor of 1.77 in Fig. 5) was observed.

5. Crucially, while the absolute maximum stress recorded *during* the impulse may not peak exactly at $\beta = 1$, this condition produces the largest amplitude of *free vibrations* after the load is removed and should be considered in models with damping. This post-impulse oscillatory response is critical for fatigue assessment and structural integrity of the magnet system.

6. The analysis confirms that for single-layer coils with long pulses, simplified static models are adequate for stress estimation. However, the developed dynamic methodology and the identified resonant behavior are essential for the design and integrity analysis of advanced magnets, particularly for multi-layer or composite systems [32] operating with fast pulses, where it can be further expanded and scaled. It should be noted that the present formulation is based on linear elasticity and a prescribed quasi-force-free force distribution. In more detailed coupled models, electromagnetic diffusion, damping, nonlinear material response at high stress levels, and deviations of the current distribution from the idealized profile may modify the quantitative values of dynamic amplification. These effects do not alter the frequency-controlled nature of the quasi-static-to-dynamic transition identified here but may influence the exact stress amplitudes in practical systems.

CRediT authorship contribution statement

Maxim I. Lobachev: conceptualization, methodology, investigation, writing – review & editing, writing – original draft, data curation.

Conflict of interest

The author declares that he has no conflict of interest.

References

1. Boriskov GV, Bykov AI, Dolotenko MI, Egorov NI, Kudasov YB, Platonov VV, Selemir VD, Tatsenko OM. Research in ultrahigh magnetic field physics. *Physics-Uspekhi.* 2011;54(4): 421.
2. Korshunov MM. Superconducting state in iron-based materials and spin-fluctuation pairing theory. *Physics-Uspekhi.* 2014;57(8): 813.
3. Bykov A, Temnikov F, Korshunov A, Kozabaranov R, Kudasov Y, Makarov I, Maslov D, Platonov V, Repin P, Strelkov I, Surdin O. Ultrahigh magnetic field study on Gd_2BaNiO_5: Suppression of the Haldane gap. *Physical Review B.* 2024;110(21): 214439.
4. Tkáč I, Benneyworth MA, Nichols-Meade T, Steuer EL, Larson SN, Metzger GJ, Uğurbil K. Long-term behavioral effects observed in mice chronically exposed to static ultra-high magnetic fields. *Magnetic Resonance in Medicine.* 2021;86(3): 1544–1559.
5. Zhang L, Hou Y, Li Z, Ji X, Wang Z, Wang H, Tian X, Yu F, Yang Z, Pi L, Mitchison TJ. 27 T ultra-high static magnetic field changes orientation and morphology of mitotic spindles in human cells. *eLife.* 2017;6: e22911.
6. Alves Z JR, Bay F. Magnetic pulse forming: Simulation and experiments for high-speed forming processes. *Advances in Materials and Processing Technologies.* 2015;1(3-4): 560–576.
7. Khvostenko PP, Anashkin IO, Bondarchuk EN, Chudnovsky AN, Kavin AA, Khvostenko AP, Kirneva NA, Kuzmin EG, Levin IV, Leonov VM, Lutchenko AV. Current status of tokamak T-15MD. *Fusion Engineering and Design.* 2021;164: 112211.
8. Ruess T. *A First 2 MW-Class (136)/170/204 GHz Multi-Frequency Gyrotron Pre-Prototype for DEMO: Design, Construction and Key Components Verification.* Germany: KIT Scientific Publishing; 2023.
9. Vu AT, de Vries PC, Carannante G, Carvalho IS, Cinque M, Gomez I, Kudlacek O, Mattei M, Moreau P, Nouailletas R, Pangione L. Progress in the iter plasma control system design. *Fusion Engineering and Design.* 2026;222: 115501.
10. Mattei M, Ambrosino R, Ariola M, De Vries P, De Tommasi G, Di Grazia LE, Gribov Y, Pangione L, Pironti A, Zabeo L. Recent developments in ITER magnetic control algorithms. *Fusion Engineering and Design.* 2026;222: 115492.
11. Battesti R, Beard J, Böser S, Bruyant N, Budker D, Crooker SA, Daw EJ, Flambaum VV, Inada T, Irastorza IG, Karbstein F. High magnetic fields for fundamental physics. *Physics Reports.* 2018;765-766: 1–39.
12. Zherlitsyn S, Wustmann B, Herrmannsdorfer T, Wosnitza J. Status of the pulsed-magnet development program at the Dresden High Magnetic Field Laboratory. *IEEE Transactions on Applied Superconductivity.* 2012;22(3): 4300603.
13. Wang S, Wu Z, Jiang S, Wang G, Huang R, Peng T. Development of Zylon-Kevlar-Zylon hybrid fiber reinforcement technology for 100T pulsed magnet at the WHMFC. *Journal of Physics: Conference Series.* 2020;30(4): 4301204.
14. Béard J, Billette J, Ferreira N, Frings P, Lagarrigue JM, Lecouturier F, Nicolin JP. Design and tests of the 100-T triple coil at LNCMI. *IEEE Transactions on Applied Superconductivity.* 2018;28(3): 4300305.
15. McDonald RD, Mielke CH, Rickel DG. *World Record Magnetic Field 100 T.* Los Alamos National Laboratory Report. Report number: 1305044, 2012.
16. Furth HP, Levine MA. Force-free coils and superconductors. *Nuclear Fusion.* 1962;2(4): 147–155.
17. Emelyanov OA, Glyavin MY, Golubev SV, Krivosheev SI, Kruchinin AI, Luchinin AG, Magazinov SG, Parfentiev AA, Shimansky SA, Shneerson GA, Voloshin KV. Quasi-force-free magnets of small volume for generators of short-wave microwave radiation. *IEEE Transactions on Applied Superconductivity.* 2023;34(5): 4900504.

18. Shneerson GA, Voloshin KV, Titkov VV, Rodin IY, Zapretilina ER, Hon TA, Hitrov NA, Ovsyannikov VS, Lantsetov A. Application of Quasi-Force-Free Winding Concept to Superconducting Magnetic Energy Storage. *IEEE Transactions on Applied Superconductivity.* 2024;34(5): 5701204.
19. Shneerson GA, Koltunov OS, Schneider-Muntau HJ, Titkov VV, Parfentjev AA. The concept of quasi-force-free magnets: theoretical substantiation, estimation of parameters, and feasibility. *Physica B: Condensed Matter.* 2004;346: 566–570.
20. Nemov AS, Lagutkina AD, Shneerson GA. A conceptual 3-D design of a non-destructive two-layer quasi-force-free magnet for megagauss field generation. *IEEE Transactions on Magnetics.* 2022;58(3): 8000609.
21. Shneerson GA, Khlybov AV, Belov AA, Nenashev AP, Parfentiev AA, Shimanskiy SA. Deformation and mechanical stresses in a magnet with thin-walled quasi-force-free winding. *Materials Physics and Mechanics.* 2022;48(3): 355–366.
22. Lobachev MI, Novokshenov AD. Solution to the Quasi-Static Axisymmetric Problem for a Single-Layer Quasi-Force-Free Magnet. *Moscow University Mechanics Bulletin.* 2025;80(5): 187–194.
23. Ghosh AK. Axisymmetric vibration of a long cylinder. *Journal of Sound and Vibration.* 1995;186(5): 711–721.
24. Keles I, Tutuncu N. Effect of anisotropy on axisymmetric dynamic response of thick-walled cylinders. *International Journal of Pressure Vessels and Piping.* 2009;86(7): 435–442.
25. Gazis DC. Exact Analysis of the Plane-Strain Vibrations of Thick-Walled Hollow Cylinders. *The Journal of the Acoustical Society of America.* 1958;30(8): 786–794.
26. Jacquot RG, Steadman JW, Rhodine CN. The Gaver-Stehfest algorithm for approximate inversion of Laplace transforms. *IEEE Circuits & Systems Magazine.* 2012;5(1): 4–8.
27. Shneerson GA, Koltunov OS, Krivosheev SI, Adamian YE, Berezkin AN, Nenashev AP, Parfentiev AA. Models of magnets with the quasi-force-free winding manufactured from the thin solid sheets or transposed conductors. *IEEE Transactions on Plasma Science.* 2010;38(8): 1731–1738.
28. Krivosheev SI, Korovkin NV, Slastenko VK, Magazinov SG. Destruction of brittle materials by microsecond pressure pulses at their formation by magnetic pulse method. *International Journal of Mechanics.* 2015;9: 293–299.
29. Krivosheev SI, Petrov YV. Testing of dynamic property of materials under microsecond duration pressure created by the pulse current generator. In: *Proceedings of international conference on megagauss magnetic field generation and related topics*. Moscow; 2002. p.112. (In Russian)
30. Krivosheev SI, Magazinov SG, Alekseev DI. On the impact of the elastic-plastic flow upon the process of destruction of the solenoid in a super strong pulsed magnetic field. *Journal of Physics: Conference Series.* 2018;946(1): 012040.
31. Krivosheev SI, Shneerson GA, Magazinov SG, Zhukov DV, Voloshin KV. Destruction threshold of ZrO2 under microsecond magnetic-pulse action. *Materials Physics and Mechanics.* 2023;51(7): 7–14.
32. Xiao H, Yin Z, Chen X, Deng Z, Wang P, Chen S, He Y. Comprehensive analyses of buckling and stress failure of high-field pulsed magnets under biaxial Lorentz force body load. *Thin-Walled Structures.* 2023;183: 110341.